Performance of Bootstrap Embedding for long-range interactions and 2D systems

Performance of Bootstrap Embedding for Long-Range Interactions and 2D Systems

Nathan Ricke, Matthew Welborn, Hong-Zhou Ye, and Troy Van Voorhis*
Department of Chemistry, Massachusetts Institute of Technology, Cambridge, MA, 02139, USA
(Dated: January 10, 2017)

Fragment embedding approaches offer the possibility of accurate description of strongly correlated systems with low-scaling computational expense. In particular, wave function embedding approaches have demonstrated the ability to subdivide systems across highly entangled regions, promising wide applicability for a number of challenging systems. In this paper, we focus on the wave function embedding method Bootstrap Embedding, extending it to the Pariser-Parr-Pople and 2D Hubbard models in order to evaluate the behavior of the method in systems that are less amenable to local fragment embedding. We find that Bootstrap Embedding remains accurate for these systems, and we investigate how fragment size, shape, and choice of matching conditions affects the results. We also evaluate the properties of Bootstrap Embedding that lead to the method's favorable convergence properties.

Introduction

Accurate electronic structure methods, such as density matrix renormalization group [1–4], full configuration interaction [5], or other high level CI methods [6–8], can provide practically exact non-relativistic solutions to chemical systems, but tend to limited to small molecules due to high computational scaling or prefactors. More approximate methods, such as Hartree-Fock (HF) [9, 10] and density functional theory (DFT) [11, 12] have proven successful for treating systems in the thousands of atoms due to low computational scaling. These methods, however, are generally unsuccessful for treating systems with large amounts of static correlation, such as transition metal oxides and Mott insulators [13, 14]. One way to bypass the trade-off between accuracy and cost is through embedding methods, which allow for the possibility of combining the advantages of two separate methods.

There are two broad approaches to the general problem of embedding. In the first, the fragment and environment are coupled through a one-particle embedding potential. An example of this is electrostatic embedding, which treats all the interactions between the component and its surroundings as classical electrostatic interactions. This method is used in quantum mechanics/molecular mechanics (QM/MM) simulations [15, 16], where the embedding potential is calculated from electrostatic and polarization interactions between the fragment and environment. A frequent use of QM/MM simulations is to model a solute of interest treated at the QM level in a solvent treated at the MM level. Another approach is DFT-in-DFT embedding [17–19], where the embedding potential is calculated from the derivative of the non-additive energy functional. DFT-in-DFT is used to embed fragments with larger basis sets and more expensive functionals within a system initially treated with a limited basis set and inexpensive functional, and has been used to treat proteins [20], solvated molecules [21], and organic molecular crystals [22]. Another possibility is to embed wave function methods within DFT, which has been applied to binding molecules to metal surfaces [23]. The approach of performing embedding with a one-particle potential has been successful for systems with little electron correlation between the fragment and environment, as the subsystems are not directly entangled with one another.

The other approach to embedding is to include the effects of entanglement between the fragment and the environment. In this category is dynamical mean-field theory (DMFT), which self-consistently embeds a local fragment Green's function within a larger bath Green's function [24–28]. Another approach is density matrix embedding theory (DMET) [29–34], which originated as a simplified approach to DMFT [30]. DMET handles correlation between the fragment and environment through a quantum bath. DMET has shown promise for treating highly correlated systems, allowing for the possibility of accurate embedding across covalent bonds, and has the advantage that it can be applied to any methods that produce density matrices. The method we will expand on in this paper, Bootstrap Embedding [35], borrows the decomposition process from DMET, but differs in the process of iteratively improving the initial ansatz.

In the literature thus far, Bootstrap Embedding has only been applied to 1D systems with local electron interactions [35]. As Bootstrap Embedding is a process that relies on a clearly defined center for each fragment, an important point of inquiry is on the quality of the method for systems that more closely resemble molecules. In this work, we apply Bootstrap Embedding to the Pariser-Parr-Pople (PPP) model [36–38] and the 2D Hubbard model [39, 40]. The PPP model includes non-local coulombic interactions that cannot be contained within a single fragment, whereas the 2D Hubbard model is more densely connected and increases the amount of interaction between the fragment and bath. Both of these effects lessen the extent to which any particular basis function within the fragment is embedded from the edges, so they are important tests for whether Bootstrap Embedding can be further generalized. In the

* tvan@mit.edu

PPP model, we address the impact of 2-electron interactions and bond length alternation, as well as energy convergence with fragment size. We find that Bootstrap Embedding effectively handles local 2-electron correlation, and that 2-electron interactions that extend beyond the fragment are accurately approximated by a mean-field treatment. In the 2D Hubbard model, we address how fragment size, fragment shape, and choice of applied constraints affect the accuracy of the method, demonstrating that specific partitioning schemes are more effective for describing the system.

Theory

A crucial component for understanding both the operation and motivation of DMET and Bootstrap Embedding is the Schmidt decomposition [41–43], which is the process by which the system is decomposed into a fragment with an entangled bath. As the Schmidt decomposition has been described generally elsewhere [29–34], we will restrict this discussion to the approach used in this paper: Schmidt decomposition of a HF solution. Given a solution to a system with N basis functions, assumed here to be orthonormal, we begin by choosing a fragment consisting of N_f orbitals. Through the Schmidt decomposition, we can decompose the full wave function of the system into

$$|\Psi\rangle = (\sum_{i}^{2^{N_f}} c_i \, |\alpha_i\rangle \, |\beta_i\rangle) \otimes |\varepsilon\rangle, \tag{1}$$

where $|\alpha_i\rangle$ are the fragment determinants, $|\beta_i\rangle$ are bath determinants, and $|\varepsilon\rangle$ are the environment determinants. The fragment merely consists of the orbitals that we chose, while the bath contains the entanglement between the fragment and the rest of the system. In the specific case of HF, the Schmidt decomposition is equivalent to a choice of active space [31]. One of the primary advantages of this decomposition is that the bath is no larger than the fragment, so the fragment may be chosen arbitrarily small and the bath will also be just as small.

So far, Eq. 1 is only an alternate form of the original wave function. We continue by taking the electronic Hamiltonian for the full system,

$$\hat{H} = \sum_{pq}^{N} h_{pq} \hat{a}_p^\dagger \hat{a}_q + \sum_{pqrs}^{N} v_{pqrs} \hat{a}_p^\dagger \hat{a}_q^\dagger \hat{a}_s \hat{a}_r, \tag{2}$$

and projecting it onto a fragment, F, and its corresponding approximate mean-field bath states to produce a new Hamiltonian in a reduced fragment-bath subspace,

$$\hat{H}^F = \sum_{ij}^{2N_f} \tilde{h}_{ij}^F \hat{r}_i^\dagger \hat{r}_j + \sum_{ijkl}^{2N_f} \tilde{v}_{ijkl}^F \hat{r}_i^\dagger \hat{r}_j^\dagger \hat{r}_l \hat{r}_k, \tag{3}$$

in a process detailed elsewhere [32, 34]. Here, the creation and annihilation operators for the full system, $\hat{a}^\dagger$ and $\hat{a}$, have been replaced with $\hat{r}^\dagger$ and $\hat{r}$ to denote creation and annihilation operators of quasi-particles within the fragment-bath systems. Note that this process includes interactions between the fragment and the environment in the diagonal elements of $\tilde{h}$. In order to improve upon this mean-field solution, we use a more accurate method within the fragment-bath reduced space to solve for the ground state of $\hat{H}^F$ to obtain the density matrix of each fragment. For this paper, we apply FCI to solve for eigenvectors of $\hat{H}^F$,

$$\hat{H}^F |\Psi^F\rangle = E^F |\Psi^F\rangle, \tag{4}$$

to obtain, in the reduced space, the 1-pdm, P^F, and 2-pdm, Γ^F, for each of the fragments.

At this point, Bootstrap Embedding diverges from DMET, as Bootstrap Embedding continues by applying a set of constraints that match density matrix elements between different fragments within the FCI space. This is motivated by the observation that, if the wave function had been exact prior to Schmidt decomposition, all density matrix elements shared by two overlapping fragments would be the same. Here we will focus only on directly matching density matrix elements one at a time. Once a set of matching conditions are chosen, they may be applied to some fragment, F, with a reduced fragment-bath space that we will denote as $\mathbb{F}$. These conditions constrain specific elements of F's 1-pdm and 2-pdm to match corresponding elements from other fragments that have more effectively embedded those specific density matrix elements:

$$\langle \Psi^F | \hat{r}_i^\dagger \hat{r}_j | \Psi^F \rangle \leftarrow P_{ij}^M \tag{5}$$

$$\langle \Psi^F | \hat{r}_i^\dagger \hat{r}_j \hat{r}_l^\dagger \hat{r}_k | \Psi^F \rangle \leftarrow \Gamma_{ijkl}^M. \tag{6}$$

The indices $ijkl$ specify all density matrix elements in fragment F that are not central, namely edge basis functions, that are selected from $\mathbb{F}$ by the function E. The elements of $E(\mathbb{F})$ are all matched to corresponding central density matrix elements that are on other fragments, specified by M, where those density matrix elements are more fully embedded. The choice of which density matrix elements to constrain is made based on the observation that the error in this embedding process comes from an inexact bath, and that basis functions that interact least strongly with the bath will have the most accurate density matrix elements.

All partitioning schemes in Bootstrap Embedding will also generally require a constraint on the populations,

$$\sum_{F, s \in C(\mathbb{F})} \langle \Psi^F | \hat{r}_s^\dagger \hat{r}_s | \Psi^F \rangle \leftarrow N_{elec}, \tag{7}$$

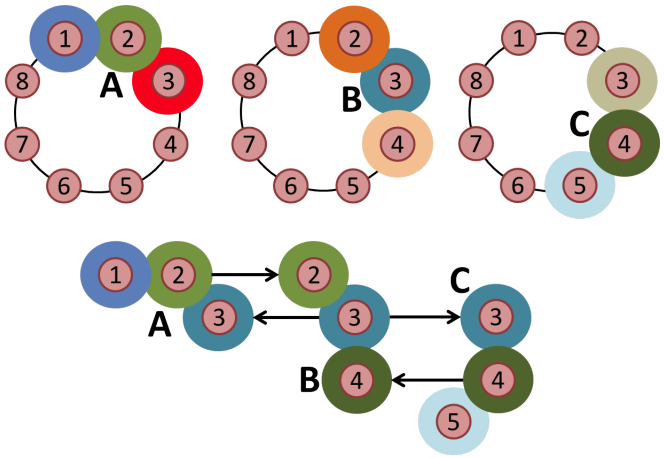

Figure 1: Three of the eight fragments for describing the asymmetric atomic ring. The arrows indicate the matching conditions imposed by these three fragments on each other. For example, atomic orbital **3** is the central orbital in fragment **B**, so the density matrix elements of orbital **3** from fragment **B** would be used to constrain the density matrix elements of orbital **3** in fragments **A** and **C**. In turn, orbitals **2** and **4** in fragment **B** are constrained by the corresponding central orbitals in fragments **A** and **C.**

where F indexes all fragments, and s indexes the central basis functions that are in F, which are selected by the function C acting on $\mathbb{F}$. It is important for this step that the partitioning scheme defines every basis function to be central in precisely one fragment.

To illustrate one particular choice of matching conditions, we consider an eight-membered, minimal basis hydrogen ring with the modification that every atomic site has a different potential, such that each site is unique (Figure 1). In fragment **B**, atomic orbital **3** is at the center of the fragment, and therefore most embedded within the fragment. As atomic orbital **3** is also in fragments **A** and **C**, the population, P_{ii}, and on-top, Γ_{iiii}, density matrix elements of orbital **3** of **A** and **C** may be matched to **B**, such that $P^A_{33} \leftarrow P^B_{33}$ and $P^C_{33} \leftarrow P^B_{33}$. This is an example where the matching conditions are well defined for the system; for other systems this may not always be the case, as will be covered further in the **Results** section.

The energy of the system is minimized, subject to the applied constraints, by solving for stationary points of the Lagrangian,

$$\begin{aligned} L[\Psi,\vec{\lambda},\vec{\Lambda},\mu] \equiv \sum_F (&\langle\Psi^F|\hat{H}^F_{emb}|\Psi^F\rangle \\ &+ \sum_{ij\in E(\mathbb{E})} \lambda_{ij}(\langle\Psi^F|\hat{r}^\dagger_i\hat{r}_j|\Psi^F\rangle - P^M_{ij}) \\ &+ \sum_{ijkl\in E(\mathbb{F})} \Lambda_{ijkl}(\langle\Psi^F|\hat{r}^\dagger_i\hat{r}_j\hat{r}^\dagger_l\hat{r}_k|\Psi^F\rangle - \Gamma^M_{ijkl}) \\ &+ \epsilon^F(\langle\Psi^F|\Psi^F\rangle - 1)) \\ &+ \mu((\sum_{F,s\in C(\mathbb{F})} \langle\Psi^F|\hat{r}^\dagger_s\hat{r}_s|\Psi^F\rangle) - N_{elec}), \end{aligned} \quad (8)$$

where the term $\langle\Psi^F|\Psi^F\rangle - 1$ is the constraint that ensures normalization, and the terms λ_{ij}, Λ_{ijkl}, μ, and ϵ^F are Lagrange multipliers. The process of applying constraints via L can be done by applying potentials to an effective Hamiltonian for each of the fragments. To show this, we begin by taking the first variation of L, namely δL, with respect to the coefficients of the FCI wave function,

$$|\delta\Psi^F\rangle \equiv \sum_I \delta c_I |\alpha_I\rangle|\beta_I\rangle, \quad (9)$$

and setting δL equal to zero:

$$\begin{aligned} \delta L = \sum_F (&\langle\delta\Psi^F|\hat{H}^F|\Psi^F\rangle + \sum_{ij\in E(\mathbb{F})} \lambda_{ij}\langle\delta\Psi^F|\hat{r}^\dagger_i\hat{r}_j|\Psi^F\rangle \\ &+ \sum_{ijkl\in E(\mathbb{F})} \Lambda_{ijkl}\langle\delta\Psi^F|\hat{r}^\dagger_i\hat{r}_j\hat{r}^\dagger_l\hat{r}_k|\Psi^F\rangle \\ &+ \mu \sum_{s\in C(\mathbb{F})} \langle\delta\Psi^F|\hat{r}^\dagger_s\hat{r}_s|\Psi^F\rangle - \epsilon^F\langle\delta\Psi^F|\Psi^F\rangle + c.c.) = 0. \end{aligned} \quad (10)$$

We can then separate out $\langle\delta\Psi^F|$ and $|\Psi^F\rangle$ from the terms shown, as well as the corresponding procedure to the complex conjugate,

$$\begin{aligned} \sum_F (\langle\delta\Psi^F|(\hat{H}^F &+ \sum_{ij\in E(\mathbb{F})} \lambda_{ij}\hat{r}^\dagger_i\hat{r}_j + \sum_{ijkl\in E(\mathbb{F})} \Lambda_{ijkl}\hat{r}^\dagger_i\hat{r}_j\hat{r}^\dagger_l\hat{r}_k \\ &+ \mu \sum_{s\in C(\mathbb{F})} \hat{r}^\dagger_s\hat{r}_s - \epsilon^F)|\Psi^F\rangle + c.c.) = 0. \end{aligned} \quad (11)$$

Since the variation is arbitrary, all terms within the square brackets must sum to 0, generating an eigenvalue equation for each fragment,

$$\begin{aligned} (\hat{H}^F &+ \sum_{ij\in E(\mathbb{F})} \lambda^F_{ij}\hat{r}^\dagger_i\hat{r}_j + \sum_{ijkl\in E(\mathbb{F})} \Lambda^F_{ijkl}\hat{r}^\dagger_i\hat{r}_j\hat{r}^\dagger_l\hat{r}_k \\ &+ \mu \sum_{s\in C(\mathbb{F})} \hat{r}^\dagger_s\hat{r}_s)|\Psi^F\rangle = \epsilon^F|\Psi^F\rangle. \end{aligned} \quad (12)$$

We can now define a new Hamiltonian that includes the terms from the constraints:

$$\begin{aligned} \hat{H^F}_{cons} = \hat{H}^F &+ \sum_{ij\in E(\mathbb{F})} \lambda_{ij}\hat{r}^\dagger_i\hat{r}_j + \\ &\sum_{ijkl\in E(\mathbb{F})}^{N_f} \Lambda_{ijkl}\hat{r}^\dagger_i\hat{r}_j\hat{r}^\dagger_l\hat{r}_k + \mu \sum_{s\in C(\mathbb{F})} \hat{r}^\dagger_s\hat{r}_s. \end{aligned} \quad (13)$$

It is now apparent in this form that the Lagrange multipliers constrain the system by acting as applied potentials to $\hat{H}^F$, with the coherence, λ_{ij}, and population, μ, constraints modifying the effective $\tilde{h}^F_{ij}$, and the two electron constraints, Λ_{ijkl}, modifying the effective $\tilde{v}^F_{ijkl}$.

Once the energy is minimized subject to constraints within the fragment-bath space, the energy of each fragment is calculated using the unmodified $\hat{H}^F$, and summed across all fragments, to evaluate the total energy of the system:

$$E = \sum_F (\sum_{sj} \tilde{h}^F_{sj} P^F_{js} + \sum_{sjkl} \tilde{v}^F_{sjkl} \Gamma^F_{klsj}). \quad (14)$$

Here, the indices jkl run over all of $\mathbb{F}$, and the index s runs over all central basis functions in $\mathbb{F}$. The overall process of Bootstrap Embedding, specialized to the case of embedding FCI in HF, is described in **Algorithm 1**.

Algorithm 1 Bootstrap Embedding

1: Input: $\hat{H}$, N_{elec}, $Tolerance$, and a partitioning scheme for the system
2: Solve HF for the full system
3: Schmidt decompose the HF solution for each fragment, and project $\hat{H}$ to $\hat{H}^F$ (Eq. 3)
4: $\hat{H}^F_{cons} = \hat{H}^F$
5: **do**
6: Solve $\hat{H}^F_{cons}$ with FCI $\forall F$, yielding P^F, Γ^F (Eq. 4).
7: $\hat{H}^{F,old}_{cons} = \hat{H}^F_{emb,cons}$
8: Using P^F and Γ^F for each F, calculate potentials requred to match central basis functions (Eqs. 5&6) and obtain the correct total population (Eq. 7), yielding $\hat{H}^F_{cons}$ (Eq. 13).
9: **while** $Norm(\sum_F (\hat{H}^F_{cons} - \hat{H}^{F,old}_{cons})) > Tolerance$
10: Calculate E (Eq. 14)

Results

Prior to this work, Bootstrap Embedding had only been applied to the Hubbard model, with Hamiltonian

$$\hat{H}_{Hubb} = t \sum_{\langle i,j \rangle} \sum_{\sigma \in \{\uparrow,\downarrow\}} \hat{a}^\dagger_{i\sigma} \hat{a}_{j\sigma} + U \sum_i \hat{n}_{i\uparrow} \hat{n}_{j\downarrow}, \quad (15)$$

where $\hat{n}$ are number operators for a given spin, t is the one-electron hopping term, and U is the two-electron, on-site repulsion. We consider how Bootstrap Embedding performs when extending the model in two distinct ways with the PPP model and the 2D Hubbard model.

PPP Model

Long range interactions cannot be entirely captured within a single fragment for local embedding methods, so an initial consideration is how long range coulombic interactions affect the accuracy of Bootstrap Embedding. We will therefore begin with presenting results from the PPP model [36–38], which models pi-electrons within conjugated polymers. The PPP model has a Hamiltonian that may be expressed as,

$$\hat{H}_{PPP} = \sum_{\langle i,j \rangle}^{N} \sum_{\sigma \in \{\uparrow,\downarrow\}} (t + \omega X_{ij}) \hat{a}^\dagger_{i\sigma} \hat{a}_{j\sigma} + U \sum_i \hat{n}_{i\uparrow} \hat{n}_{j\downarrow} + \sum_{i \neq j}^{N} V_{ijij} \hat{n}_i \hat{n}_j + \sum_{\langle i,j \rangle}^{N} k X^2_{ij}. \quad (16)$$

where the one-electron hopping term has been modified by alternation in the bond length, with X_{ij} representing the deviation of the bond length from equilibrium, such that $X_{ij} = r_{ij} - r_0$, where r_0 is the equilibrium bond length of 1.4 Å and r_{ij} is the bond length between sites i and j. The constant ω represents the sensitivity of one-electron hopping to deviations in bond length. Another term, V_{ijij}, has been added to represent long-range two electron repulsion that decays according to the Ohno potential [44],

$$|i-j| = 1\text{: } V_{ijij} = \frac{U}{\epsilon(1 + 0.6117 \text{Å}^{-2} R^2_{ij})^{1/2}} \quad (17)$$

$$|i-j| > 1\text{: } V_{ijij} = \frac{U e^{-\frac{R_{ij}}{\alpha r_0}}}{\epsilon(1 + 0.6117 \text{Å}^{-2} R^2_{ij})^{1/2}}. \quad (18)$$

The values of these variables used in this model were derived from a fit of the model to trans-polyacetylene, with $\epsilon = 2$, $\alpha = 1.9$, $t = -2.385eV$, $\omega = 2.985eV\text{Å}^{-1}$ and $U = 11.13eV$ [45, 46]. The final term, $\sum_{\langle i,j \rangle}^{N} k X^2_{ij}$, represents the bond compressibility with spring constant k. As trans-polyacetylene naturally has alternation in bond length between single and double bonds, we tuned the value of k to reproduce a bond length alternation of 0.04 Å for the exact solution of the system, yielding $k = 12.0\,\text{eV}\text{Å}^{-2}$.

It is important to note that the size of the fragment determines the type of constraints that may be applied. Fragments with one or two sites do not have bootstrapping constraints, whereas fragments with three sites or larger have either one or two most central sites that may be used to constrain on-top elements on all other sites. For fragments larger than three sites, one-electron coherence constraints may also be applied (Figure 2). Although each site within the system is identical, bond length alternation leads to two possible ways to partition the lattice for even-numbered fragments ("short-long-short" versus "long-short-long"). As illustrated in Figure 2, we resolve this for even sites by including both fragments in the partitioning scheme and constrain the edges of one fragment ("SHORT-long-SHORT") to match the center of the other ("long-SHORT-long"). For fragments with an odd number of sites there is only one unique fragment, so that while we are formally constraining

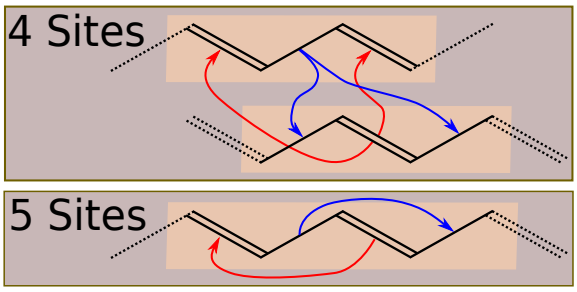

Figure 2: The one-electron coherence constraints for fragments with four and five sites. Each arrow represents a constraint that is applied from a central coherence to an edge coherence; the blue arrows indicate constraints applied between the long bonds, and the red arrows indicate constraints applied between short bonds. In the 4 site case, the central bond may be either long (top: short-long-short) or short (bottom: long-short-long) bond, so both fragments are included. Coherence constraints for 4 sites are applied from the central long bond in the top fragment to the edge long bonds in the bottom fragment, and the central short bond of the bottom fragment constrains the edge short bonds of the top. In the 5 site case, only a single unique fragment exists for the PPP model, so constraints are applied from the central coherences of the fragment to its own edge coherences.

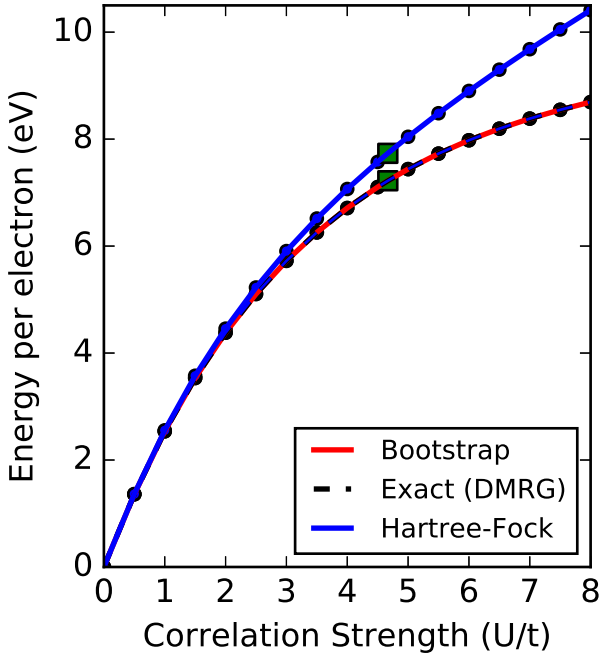

Figure 3: Correlation strength scan for a 26 site PPP model. The parameters other than U were held constant during the scan. The green square indicates the correlation strength present in the PPP model for trans-polyacetylene.

one fragment to another, in practice this can be accomplished by making the edge of the fragment ("SHORT-long-short-long") match the center ("short-long-SHORT-long"). While it is possible to define other 1-pdm and 2-pdm constraints, we chose to restrict the scope of this study to constraining coherence and on-top elements, as our earlier study demonstrated the effectiveness of each of these constraints for improving accuracy [35].

With a 5 site fragment in a 26 site PPP lattice, we scanned over correlation strength while holding the other parameters of the model constant (Figure 3). DMRG data was generated by the BLOCK DMRG code [1, 47–50] as reference data for evaluating Bootstrap Embedding in this model. The value of the energy curves were shifted such that the DMRG energy was zero at $U/t = 0$. It is apparent in Figure 3 that Bootstrap Embedding is a significant improvement over HF for the PPP model, as Bootstrap embedding remains very close to the exact result relative to HF even at $U/t = 8$. As long-range coulombic interactions not contained in the fragment are treated at the same level as HF, it appears that the significant improvement of Bootstrap Embedding over HF is indeed its ability to recover local correlation, and that approximating long-range coulombic interactions in Bootstrap Embedding does not appear to be a significant source of error. This is in line with the general observation that mean-field methods are effective for describing long-range interactions, as such interactions tend to include many terms that are well approximated by an average, validating this particular choice of approximation.

Linear polymers with half-filled pi orbitals should exhibit bond length alternation as per Peierls distortion [51], but accurately predicting the magnitude of the distortion is a challenge for electronic structure methods. To investigate this, we scanned over bond length alternation (Figure 4) over the range of $0.00 - 0.10$Å from the base bond length. This simulation was performed with a 5 site fragment in a 26 site PPP lattice with a constant $U = 11.13eV$. As can already be seen in Figure 3, the energy of the HF solution was strictly higher than the Bootstrap Embedding solution, so we shifted the HF solution to match the reference DMRG data when no bond length alternation was present such that the shapes of the curves could be more readily compared. As bond length alternation varies (Figure 4), it is apparent that Bootstrap Embedding recovers the correct shape and is very close to the energy of the exact curve, whereas even the shifted HF solution does not recover the correct shape of the exact curve. It is of particular note that Bootstrap Embedding provides a much closer prediction of equilibrium bond length alternation than HF.

While HF may initially appear as somewhat like a straw-man for this system, it is important to note that the initial ansatz was HF, and this demonstrates that Bootstrap Embedding remains accurate for this system even while its initial ansatz fails. Furthermore, the long-range coulombic interactions between the fragment and the rest of the system are treated at the HF level, indicating that the primary cause for HF's failure in the PPP model is local correlation that can be recovered at the FCI level within the fragment. This failure is not merely

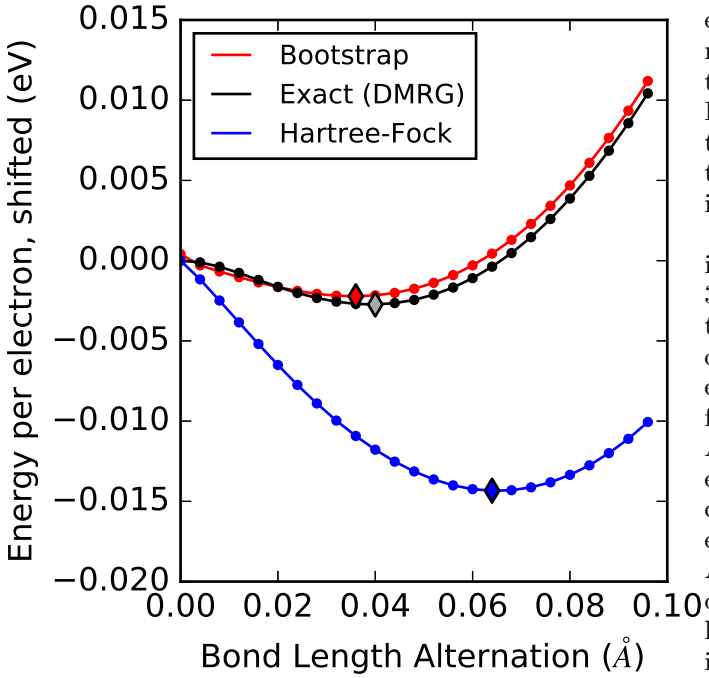

Figure 4: Bond length alternation scan for a 26 site PPP model. The parameters other than bond length alternation were held constant during the scan. The diamond along each of the curves is at the location of the minimum energy bond length alternation for that particular method.

of theoretical interest, as it is generally expected that the geometries of HF are fairly close to the correct values, but these tests show that this can be an inaccurate assumption in systems with enough electron correlation.

To investigate convergence with fragment size, we scan over occupation on a 50 site lattice for fragments sized 1 to 5, and compare the energy relative to DMRG (Figure 5). While increasing fragment size does not lead to monotonic convergence at every point in the filling scan, it does appear in Figure 5 that larger fragments visibly increase overall accuracy. To study the extent of this increase in accuracy, we plot the root mean squared difference between Bootstrap Embedding summed over all lattice fillings, and plot the convergence with fragment size (Figure 5). Analyzing this trend in Figure 5, it appears that Bootstrap Embedding appears to exhibit quasi-exponential convergence with increasing fragment size for the PPP model, similar to its performance in the 1D Hubbard model [35].

2D Hubbard Model

We applied Bootstrap Embedding to the 2D Hubbard model to evaluate its performance for 2D systems with a higher degree of connectivity, as well as a higher ratio of interfacial interactions relative to intra-fragment interactions. The increased connectivity of this model broadens the range of fragment and constraint choices, so this model is an important test of our ability to identify optimal partitioning schemes. The Hamiltonian for the 2D Hubbard model can be represented in the same form as the 1D Hubbard model in Eq. 15, with the caveat that the sum over $\langle i, j \rangle$ now refers to all four nearest neighbors in the 2D Hubbard model.

Initially using the same contiguous linear fragments as in the PPP model, we scanned over filling of a 36 by 36 lattice with $U/t = 4$. As reference data, we compare to auxiliary field quantum monte carlo (AFQMC) data on a 16 by 16 grid [52], as well as DMET data with an embedded DMRG fragment-bath solver with very large fragment sizes on a 72 by 72 grid [53]. Although the AFQMC data is not necessarily the most accurate reference data available, we use it because the data densely covers a wide range of fillings. In order to generate an energy error plot between Bootstrap Embedding data and AFQMC data, we interpolate over Bootstrap embedding data points and take the difference between the interpolated function and the reference data. Linear fragments in the 2D Hubbard do not exhibit the same exponential convergence, and it appears that little benefit is gained by increasing the fragment size beyond three sites, as the four and five site scans are not even visually distinct from one another (Figure 6). It may not be surprising, however, that embedding linear fragments of increasing size in a 2D system will yield diminishing returns, as there is likely a contribution to the error from both dimensions separately:

$$Error = Error_x(N_{frag,X}) + Error_y(N_{frag,Y}). \quad (19)$$

As $N_{frag,X}$, the number of fragment sites in the X dimension, increased while $N_{frag,Y}$ remained one, the majority of the error in this model would eventually be $Error_y$, which would explain why the error in Figure 6 rapidly converges, but to an incorrect value.

We repeated filling scan for a set of five-site fragments with different shapes (Figure 7). We chose a center site in each fragment that appeared most embedded within the fragment, and in cases where there was a most central one-electron hopping element we chose to constrain all other hopping elements to that one as well. Unlike the linear case, there was not always a clearly defined center site and hopping element for each fragment. The green fragment in Figure 7 appears to be the most accurate, but in an unexpected twist the blue fragment is not significantly better than the other fragments despite having a clearly defined central site. We reason that the advantage of the green fragment is that it minimizes fragment-bath interactions, while also enabling the application of coherence constraints that are unavailable for the blue fragment. On the other hand, the magenta and teal fragments were used to indicate that there are fragment choices that are generally inferior embedding schemes for a given system.

For a comparison between Bootstrap Embedding and

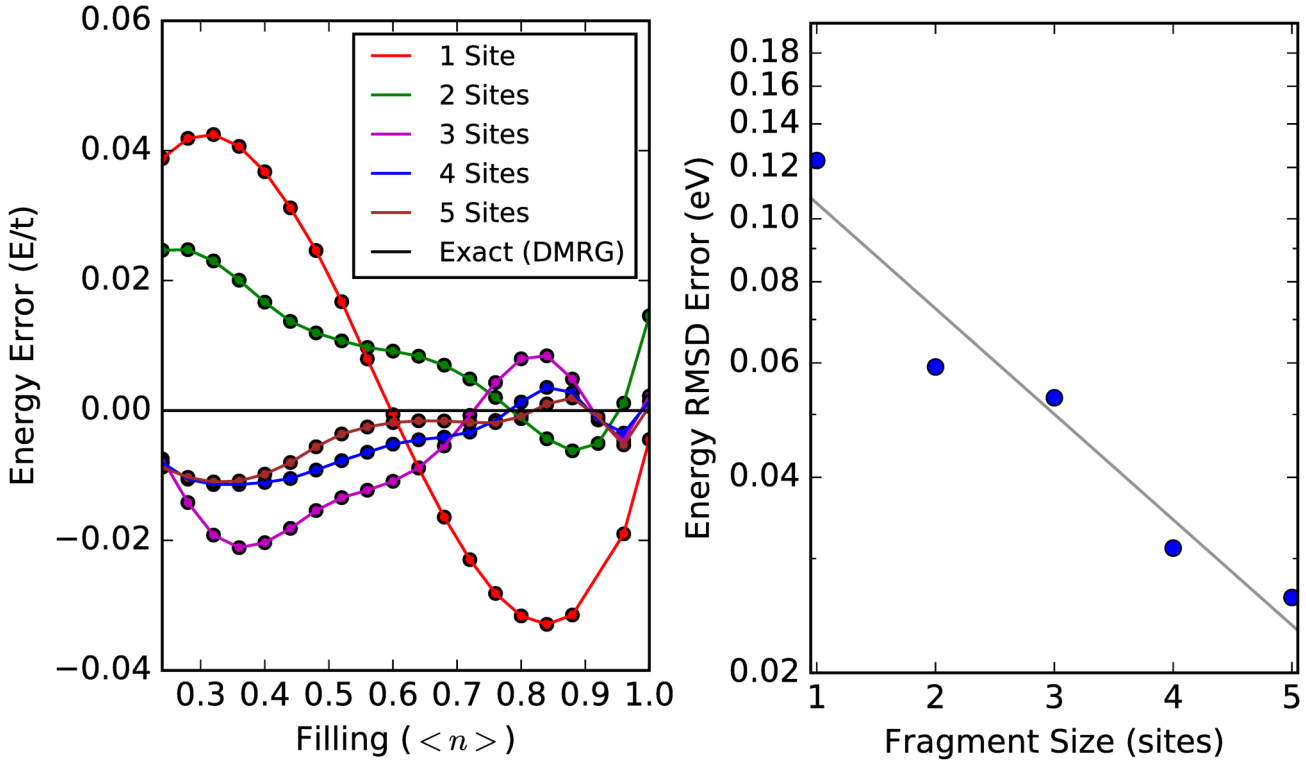

Figure 5: **A**: Bootstrap Embedding filling scan for a 50 site PPP lattice. The parameters for bond length alternation and U/t are parameterized to trans-polyacetylene. **B:** PPP Convergence with fragment size for the filling scan. DMRG calculations for the system provides the reference data.

a related method for this system, we also included data for a 2 by 2 fragment with Density Embedding Theory (DET) [33, 34]. This particular case is of note because DET and Bootstrap Embedding are equivalent for fragments in which all sites are equivalent, given that the whole system is also translationally symmetric. Even though this DET calculation is on a four-site fragment, it appears to perform similarly to sub-optimal five-site fragments with Bootstrap Embedding. This difference in accuracy is likely due to a combination of the smaller fragment size as well as the additional constraints that can be applied for larger fragments with Bootstrap Embedding.

To investigate the effect of different choices in constraints, we repeated the filling scan for one of the fragments with different choices of central site and hopping element (Figure 8). It appears that there is a significant amount of error when a site at the very end of the fragment is chosen as "central", whereas each of the three sites near the center are candidates of similar quality.

One of the most significant issues yet to be addressed for the application of Bootstrap Embedding to molecular systems is an automated process for selecting the optimal fragments and constraints that comprise a partitioning scheme. At the most fundamental level of Bootstrap Embedding, there is currently no algorithm for determining the most central basis function in a fragment. Although the choice of central site is clear in the 1D Hubbard model, there is ambiguity in the 2D Hubbard model, and this ambiguity will be amplified for 3D molecular systems with both non-local interactions and multiple basis functions per atomic site. Without a robust quantitative method for defining these constraints, application of Bootstrap Embedding to molecules would currently be limited to either the minimal basis or systems with a limited active space per atom. We also observe that the quality of fragment (Figure 7) and constraint (Figure 8) choices vary along a spectrum, and that it may not always be necessary to find the maximally optimal partitioning scheme, but merely a good one. Whether a good set may be easily determined without some quantitative metric for all systems has yet to be seen, especially given the aforementioned challenges in molecular systems.

Discussion

Bootstrap Embedding has a number of similarities to DMET, but the manner the methods differ qualitatively effects how the fragment-bath subspace evolves throughout the algorithm. In each method, the ansatz provides an initial Schmidt space after decomposition. For DMET, the process of matching terms between the mean-field density matrix and the FCI density matrix occurs by matching the FCI density matrices, P^F_{FCI}, directly to

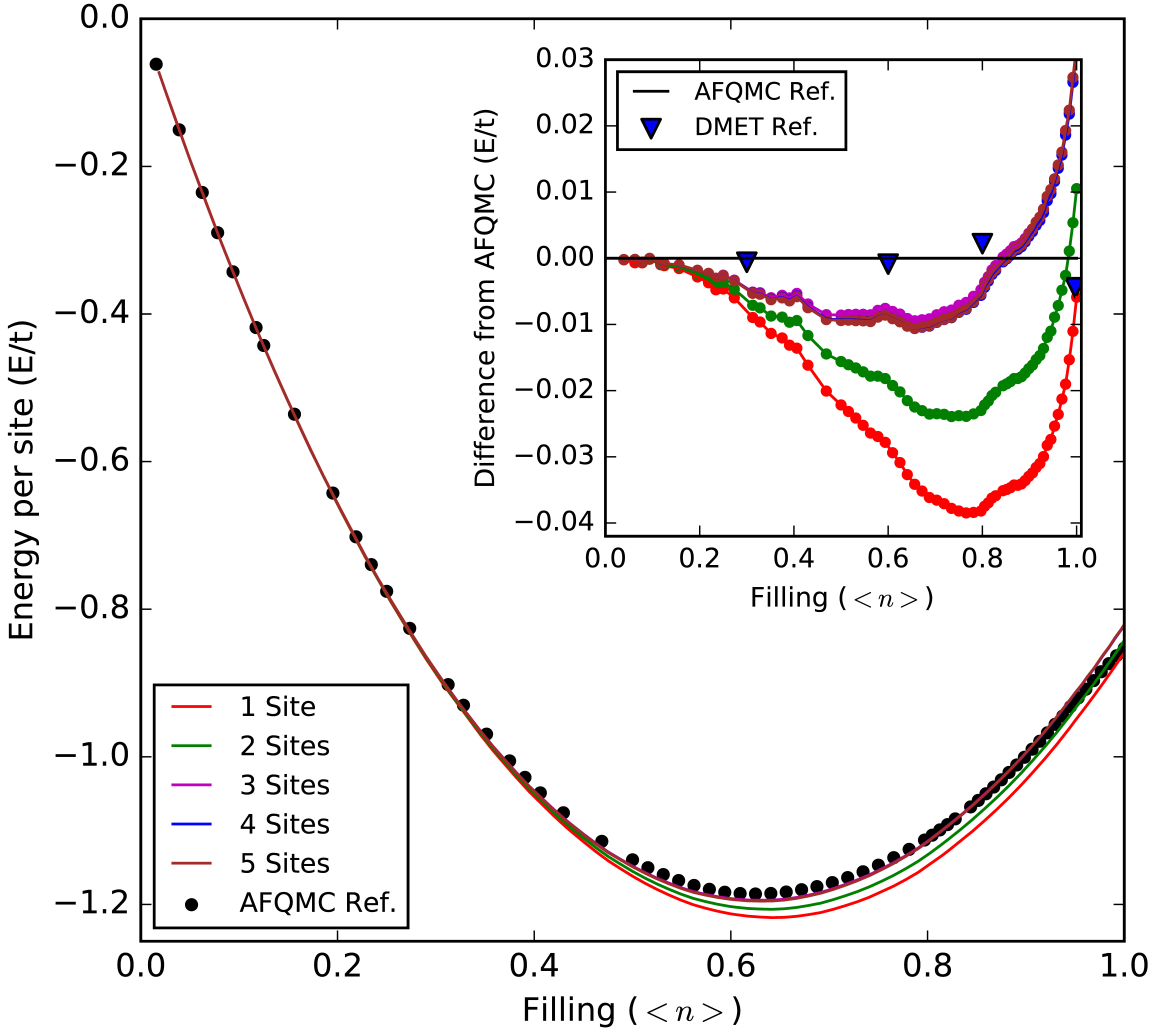

Figure 6: Filling scan for the 2D Hubbard model with linear fragments of varying sizes. Two sets of reference data were used for comparison: AFQMC data and large-fragment DMET data.

blocks of the HF density matrices corresponding to the fragment density matrices, P^F_{HF}, such that,

$$P^F_{FCI} = P^F_{HF}. \tag{20}$$

In this manner, DMET applies potentials to both the fragment and the bath, changing both of them. While this process can improve an inaccurate bath by matching it to a more accurate system, the optimization pulls both ways and can decrease the accuracy of the fragment that was formerly at the FCI level of theory. Bootstrap Embedding conversely only applies constraints to the edge density matrix elements of the fragments, and never optimizes the bath. The systems presented here have no flexibility of the mean-field solution due to translational symmetry, but for systems that do have this flexibility it would be possible to optimize the bath separately. This would amount to a minimization problem for the Lagrangian of the system similar to before (Eq. 8), with the modification that variations in the fragment wave function also includes variations in the bath by allowing the mean-field wave function used for the embedding to change:

$$|\delta\Psi^F\rangle = \sum_I \delta c_I |\alpha_I\rangle|\beta_I\rangle + \sum_I c_I |\alpha_I\rangle|\delta\beta_I\rangle \tag{21}$$

One of the advantageous properties of Bootstrap Embedding is its ease of convergence. A Newton-Raphson optimization algorithm was used for searching the Schmidt space via constraints to enforce matching conditions, generally converging in fewer than a dozen iterations for the models considered here. Analytic derivatives would certainly increase the speed of this process, and it is possible an approximate Hessian method or derivative-free method could lead to improvement if their convergence was favorable. However, it is important to emphasize that this embedding algorithm already scales very favorably with system size, and is straightforward to parallelize over a number of nodes proportional to the

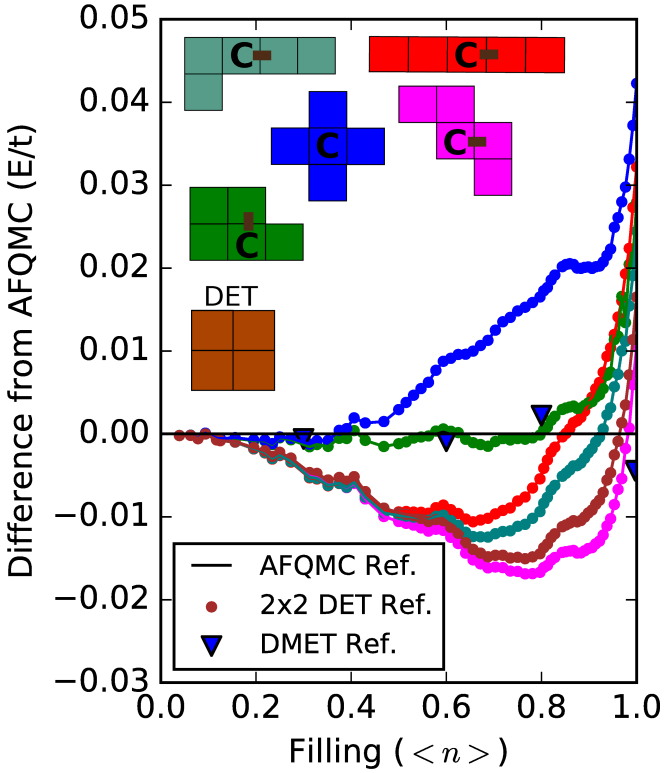

Figure 7: Filling scan for the 2D Hubbard model with nonlinear fragments of varying shapes. The **C** labels in each fragment represent the site that on-top density matrix elements were matched to, and the brown bar connecting two sites in each fragments represents the hopping element other hopping terms were matched to. DET data for a 2 by 2 fragment was included for comparison with Bootstrap Embedding. Two sets of reference data were used for comparison: AFQMC data, and large-fragment DMET data.

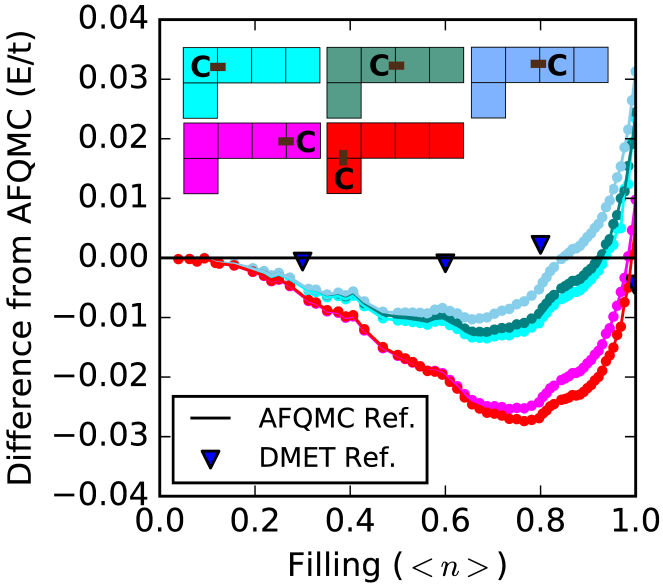

Figure 8: Filling scan for the 2D Hubbard model with varying choices of constraints. The **C** labels in each fragment represent the site that on-top density matrix elements were matched to, and the brown bar connecting two sites in each fragments represents the hopping element other hopping terms were matched to. Two sets of reference data were used for comparison: AFQMC data, and large-fragment DMET data.

number of fragments in the system.

The nature of Bootstrap Embedding's reliable convergence properties is analogous to the process of applying constraints in direct optimization methods in DFT [54, 55]. We begin with a general form of the Lagrangian L from Eq. 8, and write the applied potentials in a simplified form with all Lagrange multipliers are grouped together as $\vec{\gamma}$, with subsets $\vec{\gamma}^F$ corresponding to the multipliers within each fragment,

$$L[\vec{\gamma},\mu] \equiv \sum_F (\langle\Psi^F|\hat{H}^F|\Psi^F\rangle + \sum_i \gamma_i^F \langle\Psi^F|\hat{O}_i^F|\Psi^F\rangle) + \mu((\sum_{F,s\in C(\mathbb{F})} \langle\Psi^F|\hat{r}_s^\dagger\hat{r}_s|\Psi^F\rangle) - N_{elec}), \quad (22)$$

where γ_i^F are individual constraints from $\vec{\gamma}^F$ with corresponding weight operators, $\hat{O}_i^F$. By defining an effective Hamiltonian $\hat{H}^F(\vec{\gamma}^F) \equiv \hat{H}^F + \sum_i \gamma_i^F \hat{O}_i^F$, the Lagrangian can be rewritten as

$$L[\vec{\gamma},\mu] = \sum_F \langle\Psi^F(\vec{\gamma}^F)|\hat{H}^F(\vec{\gamma}^F)|\Psi^F(\vec{\gamma}^F)\rangle + \mu((\sum_{F,s\in C(\mathbb{F})} \langle\Psi^F|\hat{r}_s^\dagger\hat{r}_s|\Psi^F\rangle) - N_{elec}). \quad (23)$$

As we do not simultaneously optimize both μ and $\vec{\gamma}$, and it has already been shown that the optimization with a global chemical potential can be reliably performed as a local optimization problem, [54, 55] we will instead focus on the optimization problem for each fragment with respect to $\vec{\gamma}^F$. In order to understand the nature of the critical points of this constrained optimization on each fragment, we must know the second derivatives of L with respect to $\vec{\gamma}^F$. Beginning with the first derivative, we can follow the steps of the Hellmann-Feynman theorem, [56, 57]

$$\begin{aligned}\frac{\partial L}{\partial \gamma_i^F} &= \langle\frac{\partial\Psi^F}{\partial\gamma_i^F}|\hat{H}^F(\vec{\gamma}^F)|\Psi^F(\vec{\gamma}^F)\rangle + c.c. \\ &\quad + \langle\Psi^F(\vec{\gamma}^F)|\frac{\partial\hat{H}^F(\vec{\gamma}^F)}{\partial\gamma_i^F}|\Psi^F(\vec{\gamma}^F)\rangle \\ &= E\langle\frac{\partial\Psi^F}{\partial\gamma_i^F}|\Psi^F(\vec{\gamma}^F)\rangle + c.c. + \langle\Psi^F(\vec{\gamma}^F)|\hat{O}_i^F|\Psi^F(\vec{\gamma}^F)\rangle \\ &= \langle\Psi^F(\vec{\gamma}^F)|\hat{O}_i^F|\Psi^F(\vec{\gamma}^F)\rangle, \quad (24)\end{aligned}$$

where the term $\langle \frac{\partial \Psi^F}{\partial \gamma_i^F} | \Psi^F(\vec{\gamma}^F) \rangle$ and its complex conjugate are zero because it is a derivative of the norm of a wave function that has enforced normalization. Continuing with the second derivative, we obtain

$$\frac{\partial^2 L}{\partial \gamma_i^F \partial \gamma_j^F} = \langle \frac{\partial \Psi^F}{\partial \gamma_j^F} | \hat{O}_i^F | \Psi^F \rangle + \langle \Psi^F | \hat{O}_i^F | \frac{\partial \Psi^F}{\partial \gamma_j^F} \rangle. \quad (25)$$

We continue by evaluating the terms $\langle \frac{\partial \Psi^F}{\partial \gamma_j^F} | \hat{O}_i^F | \Psi^F \rangle$ and $\langle \Psi^F | \hat{O}_i^F | \frac{\partial \Psi^F}{\partial \gamma_j^F} \rangle$with first-order perturbation theory, with each yielding identical terms that transforms the equation to

$$\frac{\partial^2 L}{\partial \gamma_i^F \partial \gamma_j^F} = \sum_{A \neq 0}^{\infty} \frac{2 \langle \Psi^F | \hat{O}_i | \Psi_A^F \rangle \langle \Psi_A^F | \hat{O}_j | \Psi^F \rangle}{E_0 - E_A}. \quad (26)$$

Assuming the ground state is not degenerate, the denominator of each term in the sum is negative, as the energy of an excited state, E_A, is necessarily higher in energy than the ground state energy, E_0. Analogous to previous derivations related to this problem, if there were only a single constraint this proof would be complete: the numerator would be strictly non-negative, and the denominator strictly negative. As there are multiple constraints, however, we must first construct a matrix Ω^F of these second derivative terms,

$$\Omega_{ij}^F = \frac{\partial^2 L}{\partial \gamma_i^F \partial \gamma_j^F}, \quad (27)$$

and demonstrate that Ω^F is negative semi-definite. To show this, it is sufficient to demonstrate that for an arbitrary vector, $\vec{v}$, the value of $\vec{v} \cdot \Omega^F \cdot \vec{v}$ is non-positive. This matrix-vector product yields

$$\vec{v} \cdot \Omega^F \cdot \vec{v} = \sum_{A \neq 0}^{\infty} \frac{\langle \Psi^F | \vec{v} \cdot \vec{\hat{O}}^F | \Psi_A^F \rangle \langle \Psi_A^F | \vec{\hat{O}}^F \cdot \vec{v} | \Psi^F \rangle}{E_0 - E_A} \leq 0, \quad (28)$$

in which the terms $\langle \Psi^F | \vec{v} \cdot \vec{\hat{O}}^F | \Psi_A^F \rangle \langle \Psi_A^F | \vec{\hat{O}}^F \cdot \vec{v} | \Psi^F \rangle = ||\langle \Psi_A^F | \vec{\hat{O}}^F \cdot \vec{v} | \Psi^F \rangle||^2$ are non-negative, whereas the denominator remains negative, so all terms in the sum are non-positive. Thus, the Hessian for each fragment is negative semi-definite, meaning that the optimization is a strict maximization with at most one maximum, and no saddle points or local minima. The global optimization for applying these constraints is therefore equivalent to the far easier process of solving a local optimization problem.

Conclusions

In this work, we have more thoroughly described Bootstrap Embedding, the nature of its convergence properties, and applied Bootstrap Embedding to the PPP and 2D Hubbard models. The long range coulombic interactions in the PPP model cannot be entirely contained within the fragment, so this is an important test for the effectiveness of Bootstrap Embedding on systems with interactions more similar to molecular systems. Bootstrap Embedding appears to still capture static correlation within the PPP model to a high degree of accuracy, and also converges quasi-exponentially with increasing fragment size. Similar to the PPP model, the 2D Hubbard model is another step towards molecules, but along a different axis. Embedding is generally most accurate when the fragments have a low ratio of interfacial interactions relative to intra-fragment interactions, and higher dimensionality will generally increase the quantity of interfacial interactions. Bootstrap Embedding in particular also encounters an increasing ambiguity in the choice of a central site, such as in the 2D Hubbard model where only specifically shaped fragments have a clear set of optimal matching conditions. Presently, these limitations would restrict rigorous application of Bootstrap Embedding to molecular systems with either a minimal basis or a restricted active space on each atom. Fortunately, as seen in Figure 8, the decision between sites that qualitatively appear to be similarly embedded within the fragment does not cause a very large change in the energy, meaning that finding the absolute best central site is not always necessary. Furthermore, choosing a fragment with minimal surface interactions that allows for both coherence and on-top constraints appears more advantageous than choosing a fragment with a well defined central site (Figure 7).

As a separate branch from DMET, further developments in Bootstrap Embedding will likely follow a different, and possibly complementary, path. For systems that do not have complete translational symmetry, the mean-field solution has flexibility in the populations such that we could apply both Bootstrap Embedding as well as matching between the fragment FCI populations and mean-field solution for the full system. This sort of hybrid approach seems likely to be important for future development of Bootstrap Embedding for application to molecular systems. Another area that will require development is a systematic, ideally quantitative, method for choosing the set of matching conditions. Automated generation of matching conditions will be crucial for application to large systems with no symmetries, and particularly important for molecular systems with gaussian basis sets that may involve multiple orbitals per atomic center. Once further developed, Bootstrap Embedding could provide a low-scaling method that provides an accurate treatment of strong static correlation.

Acknowledgements

This work was funded by a grant from the NSF (CHE-1464804). T. V. is a David and Lucille Packard Foundation Fellow.

[1] G. K.-L. Chan and M. Head-Gordon, The Journal of Chemical Physics **116**, 4462 (2002).
[2] S. R. White, Physical Review Letters **69**, 2863 (1992).
[3] S. R. White and R. Noack, Physical review letters **68**, 3487 (1992).
[4] U. Schollwöck, Reviews of modern physics **77**, 259 (2005).
[5] A. Szabo and N. S. Ostlund, *Modern quantum chemistry: introduction to advanced electronic structure theory* (Courier Corporation, 1989).
[6] B. O. Roos, P. R. Taylor, P. E. Si, *et al.*, Chemical Physics **48**, 157 (1980).
[7] M. W. Schmidt and M. S. Gordon, Annual review of physical chemistry **49**, 233 (1998).
[8] R. J. Buenker, S. D. Peyerimhoff, and W. Butscher, Molecular Physics **35**, 771 (1978).
[9] D. R. Hartree, Proc. Cambridge Phil. Soc. , 111 (1928).
[10] V. Fock, Zeitschrift für Physik **61**, 126 (1930).
[11] P. Hohenberg and W. Kohn, Physical review **136**, B864 (1964).
[12] W. Kohn and L. J. Sham, Physical Review **140**, A1133 (1965).
[13] A. J. Cohen, P. Mori-Sánchez, and W. Yang, The Journal of chemical physics **129**, 121104 (2008).
[14] J. P. Perdew, International Journal of Quantum Chemistry **28**, 497 (1985).
[15] A. Warshel and M. Levitt, Journal of molecular biology **103**, 227 (1976).
[16] P. D. Lyne, M. Hodoscek, and M. Karplus, The Journal of Physical Chemistry A **103**, 3462 (1999).
[17] F. R. Manby, M. Stella, J. D. Goodpaster, and T. F. Miller, Journal of Chemical Theory and Computation **8**, 2564 (2012).
[18] J. D. Goodpaster, T. A. Barnes, F. R. Manby, and T. F. Miller, The Journal of Chemical Physics **140**, 18A507 (2014).
[19] M. E. Fornace, J. Lee, K. Miyamoto, F. R. Manby, and T. F. Miller, Journal of Chemical Theory and Computation **11**, 568 (2015).
[20] C. R. Jacob and L. Visscher, The Journal of chemical physics **128**, 155102 (2008).
[21] T. A. Barnes, J. W. Kaminski, O. Borodin, and T. F. Miller III, The Journal of Physical Chemistry C **119**, 3865 (2015).
[22] J. Neugebauer, Physics Reports **489**, 1 (2010).
[23] N. Govind, Y. A. Wang, and E. A. Carter, The Journal of chemical physics **110**, 7677 (1999).
[24] V. Turkowski, A. Kabir, N. Nayyar, and T. S. Rahman, The Journal of chemical physics **136**, 114108 (2012).
[25] W. Metzner and D. Vollhardt, Physical review letters **62**, 324 (1989).
[26] A. Georges, G. Kotliar, W. Krauth, and M. J. Rozenberg, Reviews of Modern Physics **68**, 13 (1996).
[27] A. Georges and W. Krauth, Physical review letters **69**, 1240 (1992).
[28] T. Maier, M. Jarrell, T. Pruschke, and M. H. Hettler, Reviews of Modern Physics **77**, 1027 (2005).
[29] G. Knizia and G. K. L. Chan, Journal of Chemical Theory and Computation **9**, 1428 (2013).
[30] G. Knizia and G. K. L. Chan, Physical Review Letters **109**, 1 (2012).
[31] T. Tsuchimochi, M. Welborn, and T. Van Voorhis, The Journal of chemical physics **143**, 24107 (2015).
[32] S. Wouters, C. A. Jiménez-Hoyos, Q. Sun, and G. K.-L. Chan, Journal of chemical theory and computation (2016).
[33] I. W. Bulik, G. E. Scuseria, and J. Dukelsky, Physical Review B - Condensed Matter and Materials Physics **89**, 1 (2014).
[34] I. W. Bulik, W. Chen, and G. E. Scuseria, Journal of Chemical Physics **141** (2014).
[35] M. Welborn, T. Tsuchimochi, and T. Van Voorhis, The Journal of Chemical Physics **145**, 074102 (2016).
[36] R. Pariser and R. G. Parr, The Journal of Chemical Physics **21**, 466 (1953).
[37] R. Pariser and R. G. Parr, The Journal of Chemical Physics **21**, 767 (1953).
[38] J. Pople, Transactions of the Faraday Society **49**, 1375 (1953).
[39] J. Hubbard, in *Proceedings of the royal society of london a: mathematical, physical and engineering sciences*, Vol. 276 (The Royal Society, 1963) pp. 238–257.
[40] F. H. Essler, H. Frahm, F. Göhmann, A. Klümper, and V. E. Korepin, *The one-dimensional Hubbard model* (Cambridge University Press, 2005).
[41] I. Peschel and V. Eisler, Journal of physics a: mathematical and theoretical **42**, 504003 (2009).
[42] I. Peschel, Brazilian Journal of Physics **42**, 267 (2012).
[43] I. Klich, Journal of Physics A: Mathematical and General **39**, L85 (2006).
[44] K. Ohno, Theoretica chimica acta **2**, 219 (1964).
[45] H. Fukutome, Journal of Molecular Structure: THEOCHEM **188**, 337 (1989).
[46] H. Chakraborty and A. Shukla, The Journal of Physical Chemistry A **117**, 14220 (2013).
[47] R. Olivares-Amaya, W. Hu, N. Nakatani, S. Sharma, J. Yang, and G. K.-L. Chan, The Journal of chemical physics **142**, 034102 (2015).
[48] S. Sharma and G. K.-L. Chan, The Journal of chemical physics **136**, 124121 (2012).
[49] D. Ghosh, J. Hachmann, T. Yanai, and G. K.-L. Chan, The Journal of chemical physics **128**, 144117 (2008).
[50] G. K.-L. Chan, The Journal of chemical physics **120**, 3172 (2004).
[51] R. E. Peierls, *Quantum theory of solids*, 23 (Oxford University Press, 1955).
[52] C.-C. Chang and S. Zhang, Physical Review B **78**, 165101 (2008).

[53] B.-X. Zheng and G. K.-L. Chan, Physical Review B **93**, 035126 (2016).
[54] Q. Wu and W. Yang, The Journal of chemical physics **118**, 2498 (2003).
[55] Q. Wu and T. Van Voorhis, Physical Review A **72**, 024502 (2005).
[56] H. Hellmann, *Einführung in die quantenchemie: Texte imprimé* (F. Deuticke, 1937).
[57] R. P. Feynman, Physical Review **56**, 340 (1939).